Nanoscale

Accepted Manuscript

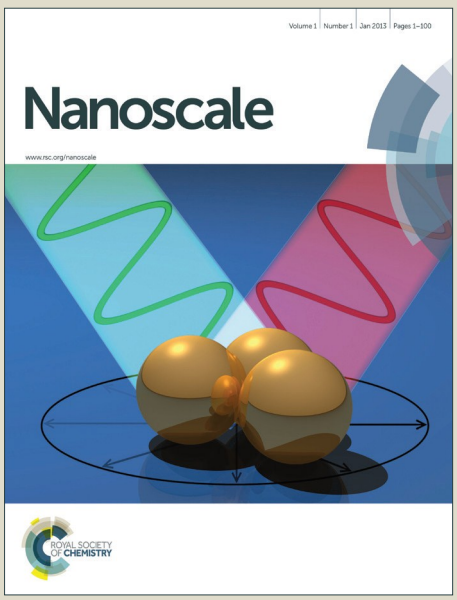

ROYAL SOCIETY OF CHEMISTRY

www.rsc.org/nanoscale

Journal Name

ARTICLE TYPE

Cite this: DOI: 10.1039/xxxxxxxxxx

Thin Film Synthesis of SbSI Micro-Crystals for Self-Powered Photodetectors with Rapid Time Response†

Karl C. Gödel,[a] and Ullrich Steiner*[a]

Received Date
Accepted Date

DOI: 10.1039/xxxxxxxxxx

www.rsc.org/journalname

We describe a new thin film deposition method for the growth of crystalline SbSI micro-needles via the conversion of Sb_2S_3 using SbI_3 vapour, in a facile process that takes less than 15 minutes. These films were used to construct photodetectors in a sandwich-type architecture, which are superior to previously reported SbSI photodetectors. The devices exhibit a detectivity of $D^* = 10^9$ Jones, a signal-to-noise ratio greater than $SNR = 10^3$ and a responsivity of $R = 10^{-5}\,\frac{A}{W}$. In time response measurements, raise and fall times of less than 8 ms and 34 ms were determined. This manufacturing method greatly simplifies the creation of fast photodetectors.

1 Introduction

Photodetectors are optoelectronic devices designed to convert light into electrical signals. They play an important role in a wide range of applications, from alarm systems and smoke detectors to consumer electronics and optocouplers for electronic circuits. Most commercial photodetectors use semiconducting materials such as Si, InGaAs, GaN or CdS. Recent research focuses however on new materials with facile deposition methods for inexpensive and scalable light sensing devices. In particular, quantum dots, polymer blends and organo-metal perovskites were investigated for photodetector applications [1,2].

The photoconductive properties of antimony sulfoiodide (SbSI) are long known [3–6]. First photoconductivity measurements using antimony sulfoiodide nanowires were presented by Nowak *et al.* in 2013 [7], which were subsequently employed for humidity sensing applications [8]. In 2015, Chen *et al.* demonstrated a SbSI photodetector based on a macroscopic single crystal [9].

Antimony sulfoiodide exhibits a series of interesting properties. It is a ferroelectric material with a Curie temperature of $T_C = 22\,^\circ$C, a high piezoelectric constant and pyroelectric properties [10]. The n-type semiconductor has an indirect band-gap of $E_g = 1.8 - 1.9\,$eV [11,12]. Theoretical calculations suggest a high charge mobility of antimony sulfoiodide caused by low effective masses of the charge carriers, making it a promising material for photovoltaic applications [12].

Here, we present a novel synthesis method for SbSI micro-crystals in a thin-film deposition route. We use this method to fabricate a SbSI photodetector with a sandwich-type architecture. This significantly improves the photodetector figures-of-merit, compared to earlier devices [9].

2 Results and Discussion

2.1 A new method for the synthesis of SbSI micro-crystals

Several synthesis routes for antimony sulfoiodide (SbSI) have been proposed in literature. Most common are a sonochemical method from elemental antimony, sulfur and iodine [8,13], hydrothermal deposition in an auto-clave [14] or chemical vapour deposition at high temperatures [15]. These methods have long processing times of 4 h and more [9,15] and result in bulk SbSI crystals.

Here, we report on a new two-step synthesis method, where SbSI micro-crystals are formed in a thin film. The first step entails the deposition of a thin film of antimony sulfide (Sb_2S_3) in a low temperature chemical bath as previously described [16,17]. The second step is the conversion of the amorphous Sb_2S_3 to crystalline SbSI using antimony iodide vapour (SbI_3). This chemical reaction was described before as part of a hydrothermal deposition method [14]

$$Sb_2S_3 + SbI_3 \longrightarrow 3\,SbSI. \quad (1)$$

To prevent oxidation of the antimony sulfide, the conversion reaction has to take place in an inert N_2 atmosphere. First, a SbI_3 evaporation target was prepared by the dissolution of SbI_3 crystals and drop-casting of the solution on a microscope slide. The substrate with pre-deposited Sb_2S_3 was mounted facing the antimony iodide target as shown in Figure S2. The target was heated to $T_t = 250\,^\circ$C within 5 min. The temperature T_t of the SbI_3 target and T_s of the substrate were recorded using a Pt100 temperature sensor (Figure S3). Within less than 5 min, an excess of antimony iodide sublimes and reacts with the Sb_2S_3 on the substrate to form SbSI. This reaction is indicated by a colour change of the

[a] Cavendish Laboratory, Department of Physics, University of Cambridge, J J Thomson Avenue, Cambridge CB3 0HE, United Kingdom.
[b] Adolphe Merkle Institute, Rue des Verdiers, CH-1700 Fribourg, Switzerland. E-mail: ullrich.steiner@unifr.ch

† Electronic Supplementary Information (ESI) available. See DOI: 10.1039/b000000x/

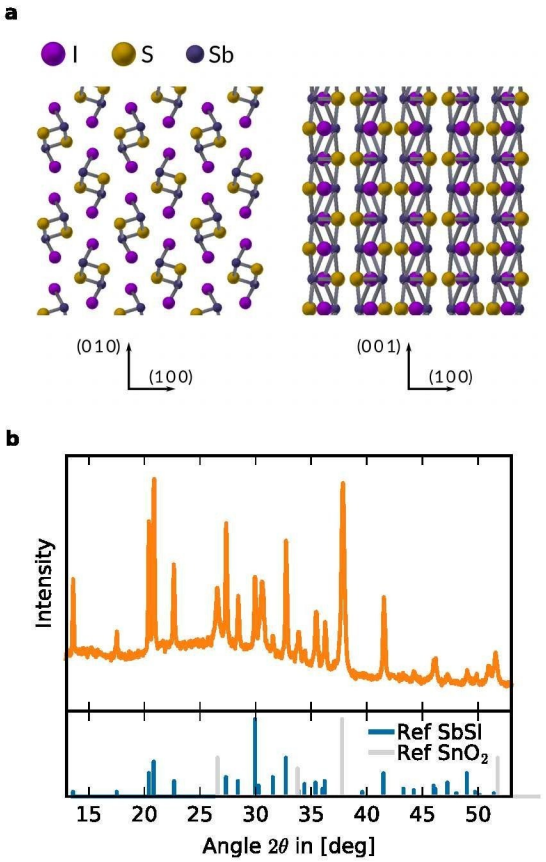

Fig. 1 (a) Schematic crystal structure of SbSI, showing long chains along the (001)-axis, which causes the preferential growth into crystal needles. (b) XRD pattern of as-prepared SbSI samples in comparison with reference patterns for SbSI and SnO_2.

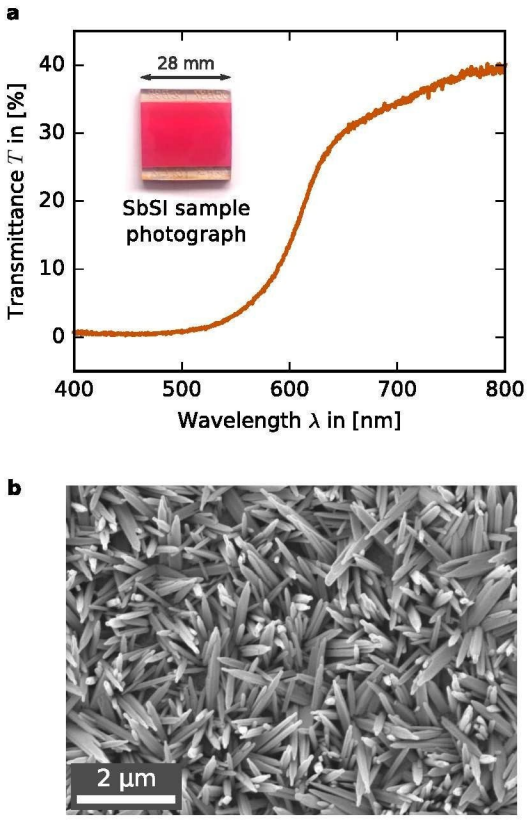

Fig. 2 (a) Transmittance spectrum of a SbSI film on a quartz substrate measured using an integrating sphere. The inset shows a photograph of the SbSI sample. (b) Top view scanning electron microscopy (SEM) image of as-prepared SbSI micro-crystals.

sample from bright orange to dark red. To increase the crystallinity, the SbSI sample was heated for another 10 min. After cooling, the samples were rinsed in ethanol to remove residual SbI_3.

To confirm the formation of crystalline SbSI, the films were characterised by x-ray diffraction (XRD) and UV-vis spectroscopy. As schematically shown in Figure 1a, antimony sulfoiodide has an orthorhombic crystal lattice, consisting of long chains along the (001)-axis. This anisotropy leads to the preferential growth of SbSI into needle like crystals. Figure 1b shows the XRD pattern of SbSI films as-deposited on a fluorine doped tin oxide (FTO) covered glass substrate. The peaks are in good agreement with the reference pattern for antimony sulfoiodide (JCPDS-ICCD PDF 00-021-0050). Additional peaks can be attributed to tin oxide (JCPDS-ICCD PDF 00-046-1088) originating from the FTO layer of the substrate. The absence of other peaks, in particular those of Sb_2S_3, indicates the formation of pure crystalline SbSI. The intensive scattering peak between $18° - 35°$ is caused by the FTO-glass substrate as confirmed by a reference measurement (Figure S4).

The band-gap of SbSI was reported to lie at $E_g = 1.9\,\text{eV}$ [12]. The onset for the absorption should therefore be at a wavelength of $\lambda_g = \frac{hc}{E_g} \approx 650\,\text{nm}$. The transmittance onset of the UV-vis spectrum in Figure 2a is in good agreement with this value. Due to the micro-structure of the SbSI film, the samples exhibit strong light scattering and the diffuse transmittance spectrum had therefore to be recorded using an integrating sphere. The inset in Figure 2 a shows the typical red colour of the SbSI samples. A comparison to the amorphous Sb_2S_3 sample before the conversion process with SbI_3 is shown in Figure S1.

The microscopic structure was further investigated using scanning electron microscopy (SEM). Figure 2b confirms the needle like morphology of SbSI crystals. The length of the individual crystals lies between $1 - 5\,\mu\text{m}$. The width of the needles is on the order of $10 - 100\,\text{nm}$. Cross-sectional SEM images (Figure S6) suggest a preferred orientation: The needles grow preferentially perpendicular to the surface, which might be induced by the roughness of the underlying FTO substrate [18]. Note that the initial Sb_2S_3 film is flat (Figure S5).

2.2 Fabrication of SbSI photodetectors with a sandwich-type architecture

Our new SbSI micro-crystal deposition method was used to fabricate functional optoelectronic devices. Earlier approaches to harness the photoconductive properties of SbSI in humidity-sensors and photodetectors [7–9] were based on devices with macroscopic electrode spacings ($0.1 - 1\,\text{mm}$). These large spacings limits

both, the maximum photocurrent signal and the time response of the detector. We have instead fabricated photodetectors with a sandwich-type architecture by contacting the SbSI crystals with an electrode spacing of less than 2 µm.

The fabrication process of the device is schematically shown in Figure 3a. The first two steps (Step 1 and 2) show the deposition of antimony sulfide and the conversion to SbSI micro-crystals by SbI_3, as described above. Then, an insulating buffer layer was deposited by spin-coating of poly(methyl methacrylate) (PMMA) from chlorobenzene with a concentration of $100\,\frac{\mathrm{mg}}{\mathrm{ml}}$ (Step 3). Process optimisation revealed that one layer of PMMA is often not sufficient to prevent shorting between the top and the bottom electrodes, thus two layers were spun-on subsequently. This PMMA layer entirely covered the SbSI crystals, preventing electrical contact with the top electrode. To partly etch the PMMA layer to reveal the tips of the crystals, pure chlorobenzene was dynamically spin-coated (Step 4). Finally, a gold metal electrode was deposited by electron beam evaporation (Step 5). A cross sectional SEM image of the final photodetector is shown in Figure 3b. For clarity, a sketch of the device is shown in Figure 3c. This schematic illustrates the working principle of the photodetector. Photons with energies higher than the band-gap of SbSI are absorbed by the detector, generating charge carrier pairs. These are preferentially transported along the (001) axis of the crystal needles, driven by an external applied electric field (generated by a bias voltage V_b). The density of free charge carriers is dependent on the intensity of the incident light, resulting in a variable photocurrent as electrical output signal.

2.3 Characterization of SbSI photodetectors

Figure 4 a shows the current-voltage characteristics of the photodetector in the dark (blue squares) and under white light illumination of a solar simulator with an irradiance of $E_\mathrm{e} = 100\,\frac{\mathrm{mW}}{\mathrm{cm}^2}$ (yellow circles). Each voltage step was followed by a 30 s stabilisation period. Note that the photodetector has a photocurrent of approx. $I = 40\,\mathrm{nA}$ even under zero bias $V_\mathrm{b} = 0\,\mathrm{V}$. This probably arises from the use of two different electrode materials, namely FTO on the bottom and gold on the top. The two electrodes have different work functions, causing a built-in potential. To further investigate this, symmetric photodetectors with an additional thin gold-layer on top of the FTO electrode were fabricated. In these devices, the short circuit current under zero bias was considerably reduced, by approximately one order of magnitude (Figure S10).

The asymmetric device is thus be self-powered and can be used without an externally applied voltage. Figure S7 in the Supporting Information shows the spectral response and the irradiance dependence of the SbSI photodetector at $V_\mathrm{b} = 0\,\mathrm{V}$. Signal-to-noise ratio, detectivity and responsivity for the device in self-powered mode ($V_\mathrm{b} = 0\,\mathrm{V}$) are shown in Figure S8.

In the following, the photodetector was operated under a bias of $V_\mathrm{b} = 100\,\mathrm{mV}$, since low operating voltages are preferable in applications and the device shows an optimal signal-to-noise ratio in this low bias region (Figure S9). The linear response of the SbSI photodetector under different illumination intensities E_e is shown in Figure 4b. The solid line is a linear least square fit, indicating the high linearity of the output signal as a function of the illumination irradiance.

The performance of the photodetectors was determined in terms of the standard figures-of-merit. These include the signal-to-noise ratio *SNR*, which is defined as [19]

$$SNR = \frac{I_\mathrm{light} - I_\mathrm{dark}}{I_\mathrm{dark}}, \tag{2}$$

where I_light and I_dark are the measured currents under illumination and in the dark, respectively. Figure 4c (top) shows the *SNR* as a function of E_e. The *SNR* value at an irradiance of $E_\mathrm{e} = 1\,\frac{\mathrm{mW}}{\mathrm{cm}^2}$ is declared as the linear dynamic range *LDR*, typically given in units of decibel (dB),

$$LDR = 20\,\mathrm{dB} \cdot \log_{10}\left(\frac{I_\mathrm{light}(E_\mathrm{e} = 1\,\frac{\mathrm{mW}}{\mathrm{cm}^2})}{I_\mathrm{dark}}\right). \tag{3}$$

The here manufactured photodetectors achieve a linear dynamic range of $LDR = 35\,\mathrm{dB}$ at a bias voltage of $V_\mathrm{b} = 100\,\mathrm{mV}$. The responsivity R is a measure for the electrical output per optical input. It is defined as [20,21]

$$R = \frac{I_\mathrm{light} - I_\mathrm{dark}}{E_\mathrm{e} A}, \tag{4}$$

where A is the active area of the photodetector ($A = 0.12\,\mathrm{cm}^2$). Figure 4c (middle) shows the responsivity R as a function of E_e for $V_\mathrm{b} = 100\,\mathrm{mV}$. The values are on the order of $R = 10^{-5}\,\frac{\mathrm{A}}{\mathrm{W}}$.

The ability of a photosensor to detect small signals is measured by the specific detectivity [19]

$$D^* = \frac{\sqrt{A\,f}R}{I_\mathrm{n}}, \tag{5}$$

where f is the electrical frequency bandwidth of the detector. Assuming that the noise current I_n is dominated by the shot noise of the dark current I_dark, the specific detectivity can be written as [1]

$$D^* = \frac{\sqrt{A}R}{\sqrt{2\mathrm{e}I_\mathrm{dark}}}, \tag{6}$$

where e is the elementary charge. The specific detectivity D^* is measured in Jones ($1\,\mathrm{Jones} = 1\,\frac{\mathrm{cm}}{\mathrm{W}\sqrt{\mathrm{s}}}$). For the photodetector described here, the specific detectivity is on the order of $D^* = 10^9$ Jones for a bias voltage of $V_\mathrm{b} = 100\,\mathrm{mV}$, plotted as a function of E_e in Figure 4c (bottom).

Compared to previously published SbSI photodetectors, the figures-of-merit of our devices are significantly improved. The maximum signal-to-noise ratio is nearly doubled and the specific detectivity is enhanced by a factor of three compared to the best previous device [9]. The figures-of-merit in self-powered mode without applied bias voltage ($V_\mathrm{b} = 0\,\mathrm{V}$) are on the same order of magnitude (Figure S8).

For many optical sensing applications, short response times to changing light signals are essential. We used an array of white light LEDs pulsed by a function generator with a rectangular waveform and measured the current response of the SbSI devices using an Autolab potentiostat in fast chronoamperometry mode with a bias voltage of $V_\mathrm{b} = 100\,\mathrm{mV}$.

Figure 5a shows the photocurrent response to a modulated

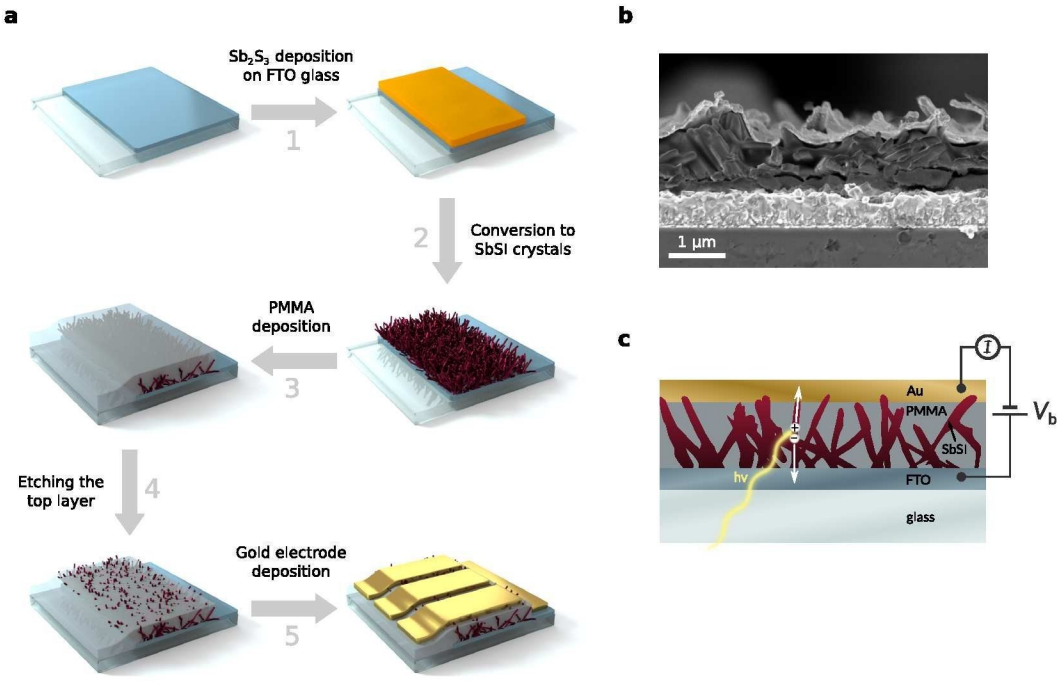

Fig. 3 (a) SbSI photodetector fabrication process in 5 steps. (b) Cross sectional SEM micrograph of a SbSI photodetector. (c) Illustration of the working principle of the photodetector. The illumination direction is from the bottom.

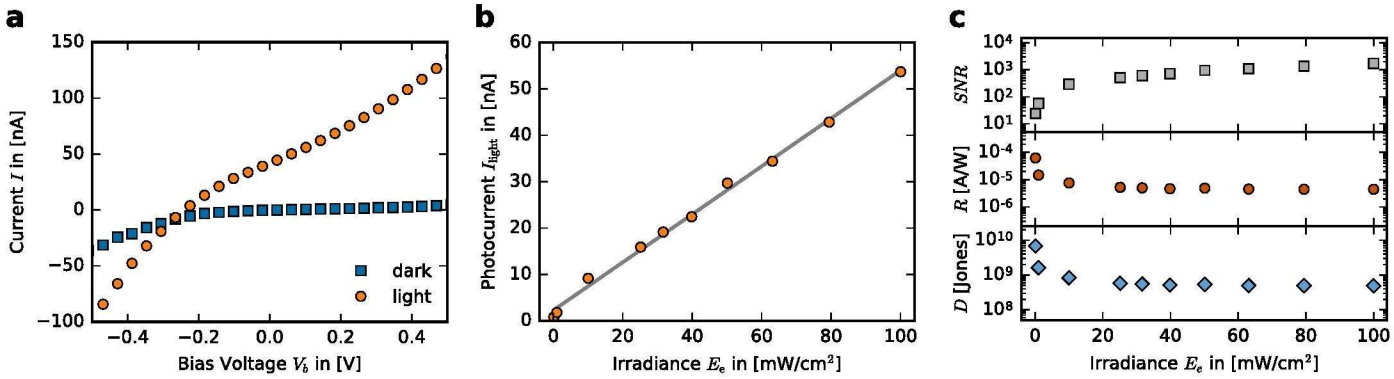

Fig. 4 (a) I-V-characteristic of the SbSI photodetector. (b) Photocurrent I_{light} as a function of the illumination irradiance E_{e}. (c) Signal-to-noise ratio SNR, responsivity R and specific detectivity D^* as a function of E_{e} at a bias voltage of $V_{\mathrm{b}} = 100\,\mathrm{mV}$.

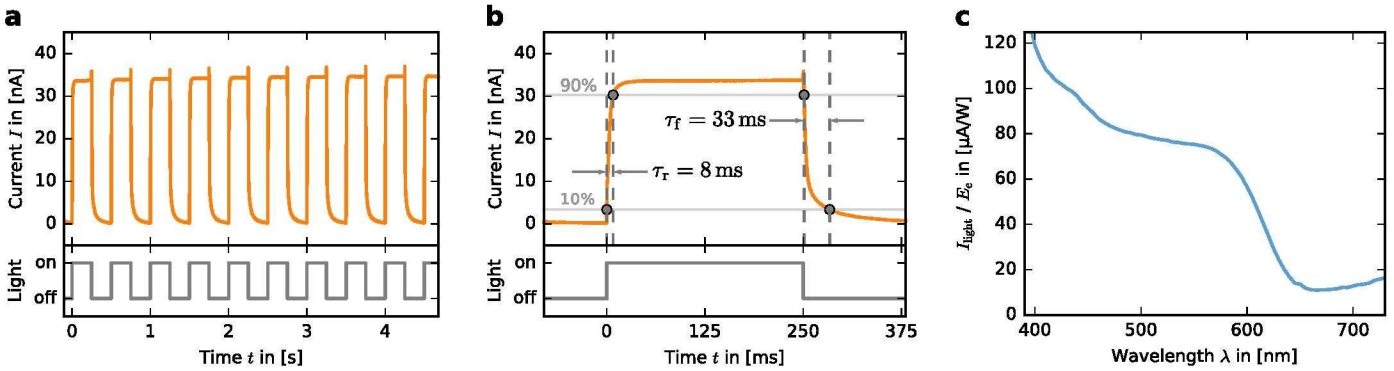

Fig. 5 (a) Time response of the photocurrent, measured for a modulated light signal shown in the lower frame. The LED array modulated with a frequency of $f = 2\,\mathrm{Hz}$ and an irradiance of $E_{\mathrm{e}} = 80\,\frac{\mathrm{mW}}{\mathrm{cm}^2}$. (b) Detailed view of one modulation cycle, showing the rise-time τ_{r} and fall-time τ_{f}. (c) Spectral response of the photodetector. The photocurrent was normalised by the irradiance of the light signal of the monochromator for each wavelength step.

light signal with a frequency of $f = 2\,\mathrm{Hz}$ with a peak intensity of $E_e = 80\,\frac{\mathrm{mW}}{\mathrm{cm}^2}$. A detailed view of one modulation cycle is shown in Figure 5b. The rise (fall) time τ_r (τ_f) is the current increase (decrease) from 10 % (90 %) to 90 % (10 %) of the maximum signal [19]. Averaged over ten modulation cycles, values of $\tau_r = 7.4 \pm 0.4\,\mathrm{ms}$ and $\tau_f = 33.8 \pm 1.5\,\mathrm{ms}$ were determined, where the errors are the standard deviations. τ_r is two orders of magnitudes and τ_f one order of magnitude faster compared to previously reported SbSI photodetectors [9].

The time response of a photoconductive light sensor under bias is dominated by the drift time of the charge carriers and the RC constant of the device [22]. The significant improvement in time response of our photodetector can be explained by its sandwich-type architecture. The short electrode distance of $1-2\,\mu\mathrm{m}$ leads to a high electric field E at a given bias voltage. As the drift velocity v_d of charge carriers increases with the electric field ($v_d = -\mu E$, where μ is the charge carrier mobility), the time response of our photodetector benefits from the small thickness of its active layer. As the active area $A = 0.12\,\mathrm{cm}^2$ is relatively large for a light sensor, the time constants could be even further improved by reducing the area and hence the *RC* constant. This would however also lead to a decrease of the current output. Higher bias voltages V_b can also further improve fall- and rise-times, but at the cost of an increased noise current and hence a decreased signal-to-noise ratio *SNR*.

Figure 5c shows the spectral response of the photodetector at a bias voltage of $V_b = 100\,\mathrm{mV}$, by plotting the measured photocurrent as a function of wavelength, normalised by the light intensity. A tungsten halogen lamp, a grating monochromator and a calibrated photodiode were used for this measurement. The output current has a clear onset at $\lambda = 650\,\mathrm{nm}$, which corresponds well to the reported band-gap energy for antimony sulfoiodide of $E_g = 1.9\,\mathrm{eV}$ [12] and further agrees with the UV-vis spectrum in Figure 2a. It shows that the detector is sensitive to most of the visible spectrum from red to blue. The spectral response at zero bias is shown in the Supporting Information (Figure S7).

3 Conclusion

We introduce a new method for the deposition of SbSI needle-shaped micro-crystals via the evaporation of SbI_3 onto amorphous Sb_2S_3. The conversion process is facile and fast, with complete conversion in under 15 min. SbSI covered substrates were employed in the fabrication of sandwich-type photodetectors. Optoelectronic investigations showed remarkable improvements compared to previously published SbSI light sensors [9]. In particular, the response and recovery time of these photodetectors is improved by one to two orders of magnitude. A promising specific detectivity of more than $D^* = 10^9$ Jones, a responsivity $R = 10^{-5}\,\frac{\mathrm{A}}{\mathrm{W}}$ and a high signal-to-noise ratio of more than $SNR = 10^3$ show that SbSI sandwich architectures are promising for the manufacture of efficient and low-cost light detectors. This is further substantiated in Table S1, where SbSI photodetectors, a perovskite and a high performance CdSe-nanowire photodetector are compared.

4 Experimental Section

4.1 Photodetector fabrication

The sample preparation steps are illustrated in Figure 3a. All chemicals were purchased from Sigma-Aldrich and used without further purification. The FTO substrate ($15\,\Omega/\square$) was cleaned by sonicating in acetone and ethanol and then partly etched using a 2 M solution of HCl and zinc powder to prevent shorting during the measurements. Amorphous Sb_2S_3 was deposited in a low-temperature aqueous chemical bath as described elsewhere [16,17]. Anhydrous SbI_3 crystals were dissolved in anhydrous ethanol at a concentration of $10\,\mathrm{mg/ml}$. 2 ml of the solution were spread on a microscope slide at 100 °C to evaporate the ethanol. This way, a thin, uniform layer of SbI_3 was formed, which was used as target for evaporation.

The target was placed onto a hotplate (Stuart CD162) in an inert atmosphere and covered by a 15 mm heigh petri-dish (see Figure S2). The Sb_2S_3-covered FTO sample was fixed to the bottom of this petri-dish, facing the SbI_3 target. The temperature of the hotplate was ramped to 250 °C within 5 min and held at this temperature for 10 min. The evaporation of SbI_3 was observable by the condensation on the petri-dish. Within the first 5 min, the colour of the sample changed from orange to dark red, indicating the formation of SbSI crystals.

The samples were left to cool under inert atmosphere. They were then rinsed in absolute ethanol to remove excess SbI_3. A PMMA film was applied onto the SbSI-covered substrate by spin-coating of a $100\,\mathrm{mg/ml}$ PMMA solution in chlorobenzene (Laurell Spin Coater Model WS-650MZ-23NPP). To increase the thickness of the polymer film, two layers are spin-coated subsequently at 4000 rpm. As a third step, pure chlorobenzene is dynamically spin-coated to remove the top layer of PMMA, to provide contact of the SbSI crystal needles with the counter-electrode. These electrodes were deposited by evaporating a 100 nm thick layer of gold using a Kurt J. Lesker e-beam evaporator.

4.2 Material characterisation

Optical transmission measurements were carried out using an Ocean Optics USB 2000 spectrometer and an integrating sphere. A Bruker D8 θ/θ (fixed sample) spectrometer with a LynxEye position sensitive detector and a standard SC detector with auto-absorber and graphite 2nd beam monochromator were used to measure X-ray diffraction patterns. The set-up operates in reflection mode and uses a Bragg Brentano parafocusing geometry. Scanning electron microscopy images were recorded using a Leo Gemini 1530 VP SEM.

4.3 Optoelectronic measurements

Current-Voltage characteristics were measured under a solar simulator from ABET Technologies (Model 11016 Sun 2000) with a xenon arc lamp and recorded using a Keithley 2635 sourcemeter controlled by a Python program. The intensity of the solar simulator was calibrated to $100\,\frac{\mathrm{mW}}{\mathrm{cm}^2}$ using a silicon reference cell from Czibula & Grundmann (FHG-ISE, RS-OD4). To alter the irradiance, neutral density filters from Thorlabs (NEK01S) were

employed.

The spectral response measurements were carried out using a 250 W tungsten halogen lamp and an Oriel Cornerstone 130 monochromator. The photocurrent was measured by a Keithley 2000 Measurement Unit. For the time response measurements, light from an array of white LEDs was focused onto the sample. The light was modulated by a Hewlett Packard 33120A function generator and the response of the photodetector was measured with an Metrohm Autolab PGSTAT302N potentiostat and recorded using the Nova software (version 1.11). The intensity of the LEDs was calibrated by measuring the photocurrent in a non-modulated mode.

Acknowledgements

K.C.G. thanks Corpus Christi College Cambridge, the Mott Fund for Physics of the Environment and the Cambridge Trust for funding. Further, we thank Bart Roose for useful discussions, Olimpia Onelli for her help with the measurements using the integrating sphere and Johnathan Lim for the FTO reference XRD pattern. This work was supported by the Swiss National Science Foundation (National Research Programme Bioinspired Materials) and the Adolphe Merkle Foundation.

References

1 L. Dou, Y. M. Yang, J. You, Z. Hong, W.-H. Chang, G. Li and Y. Yang, *Nature Communications*, 2014, **5**, 5404.

2 H. Lu, W. Tian, F. Cao, Y. Ma, B. Gu and L. Li, *Advanced Functional Materials*, 2016, **26**, 1296–1302.

3 R. Nitsche and W. J. Merz, *Journal of Physics and Chemistry of Solids*, 1960, **13**, 154–155.

4 A. Bhalla, *Ferroelectric Materials and Their Applications to Sensors*, CRC Press, 1988.

5 M. Nowak, P. Szperlich, A. Kidawa, M. Kepinska, P. Gorczycki and B. Kauch, author, 2003, pp. 172–177.

6 P. Kwolek, K. Pilarczyk, T. Tokarski, J. Mech, J. Irzmański and K. Szaciłowski, *Nanotechnology*, 2015, **26**, 105710.

7 M. Nowak, Ł. Bober, B. Borkowski, M. Kepinska, P. Szperlich, D. Stróż and M. Sozańska, *Optical Materials*, 2013, **35**, 2208–2216.

8 M. Nowak, A. Nowrot, P. Szperlich, M. Jesionek, M. Kepinska, A. Starczewska, K. Mistewicz, D. Stróż, J. Szala, T. Rzychoń, E. Talik and R. Wrzalik, *Sensors and Actuators A: Physical*, 2014, **210**, 119–130.

9 G. Chen, W. Li, Y. Yu and Q. Yang, *RSC Advances*, 2015, **5**, 21859–21864.

10 A. S. Bhalla, R. E. Newnham, L. E. Cross, J. P. Dougherty and W. A. Smith, *Ferroelectrics*, 1981, **33**, 3–7.

11 M. Nowak, B. Kauch and P. Szperlich, *Review of Scientific Instruments*, 2009, **80**, 046107.

12 K. T. Butler, J. M. Frost and A. Walsh, *Energy & Environmental Science*, 2015, **8**, 838–848.

13 M. Nowak, P. Szperlich, Ł. Bober, J. Szala, G. Moskal and D. Stróż, *Ultrasonics Sonochemistry*, 2008, **15**, 709–716.

14 Q. Yang, K. Tang, C. Wang, B. Hai, G. Shen, C. An, C. Zhang and Y. Qian, *Journal of Crystal Growth*, 2001, **233**, 774–778.

15 H. K. Dubey, L. Deshmukh, D. Kshirsagar, M. Sharon and M. Sharon, *QScience Connect*, 2013, 40.

16 M. T. S. Nair, Y. Pena, J. Campos, V. M. Garcia and P. K. Nair, *Journal of The Electrochemical Society*, 1998, **145**, 2113–2120.

17 K. C. Gödel, Y. C. Choi, B. Roose, A. Sadhanala, H. J. Snaith, S. I. Seok, U. Steiner and S. K. Pathak, *Chemical Communications*, 2015, **51**, 8640–8643.

18 J. Varghese, C. O'Regan, N. Deepak, R. W. Whatmore and J. D. Holmes, *Chemistry of Materials*, 2012, **24**, 3279–3284.

19 P. G. Datskos and N. V. Lavrik, *Encyclopedia of Optical Engineering*, 2003, 349–357.

20 M. Gong, A. Kirkeminde, Y. Xie, R. Lu, J. Liu, J. Z. Wu and S. Ren, *Advanced Optical Materials*, 2013, **1**, 78–83.

21 R. Huang, J. Zhang, F. Wei, L. Shi, T. Kong and G. Cheng, *Advanced Functional Materials*, 2014, **24**, 3581–3586.

22 M. Razeghi and A. Rogalski, *Journal of Applied Physics*, 1996, **79**, 7433–7473.

23 A. Littig, H. Lehmann, C. Klinke, T. Kipp and A. Mews, *ACS Applied Materials & Interfaces*, 2015, **7**, 12184–12192.

Supporting Information

Fig. S1 Photograph of an amorphous Sb_2S_3 sample and a SbSI sample after conversion with SbI_3 and rinsing in ethanol.

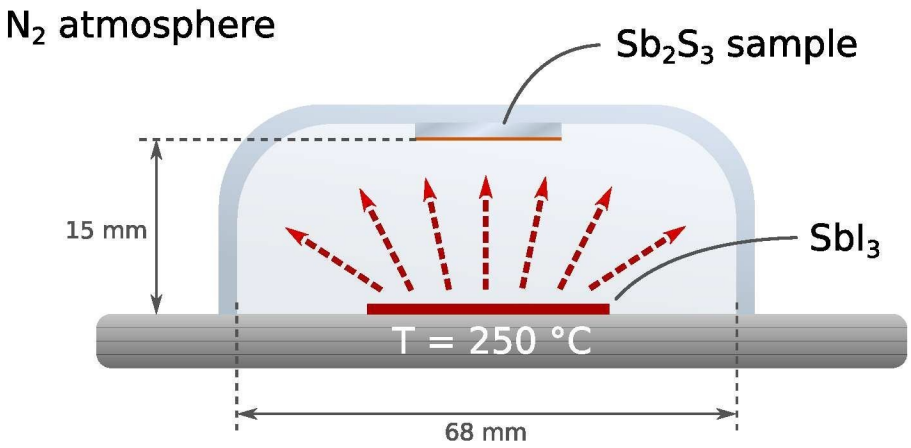

Fig. S2 Schematic of the evaporation procedure to convert amorphous Sb_2S_3 to crystalline SbSI. The conversion process is complete after only 15 min.

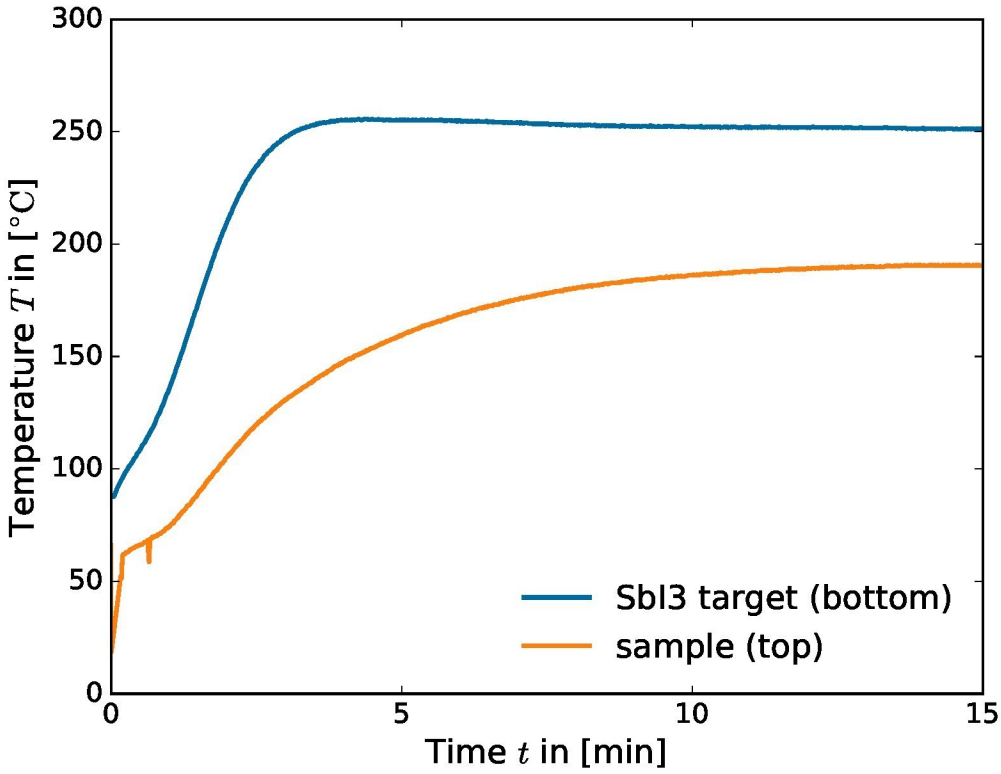

Fig. S3 Temperature curve of the SbI_3 target on the hot plate (blue), and the sample at the top of the reaction chamber (yellow). The temperatures were measured using a Pt100 temperature sensor.

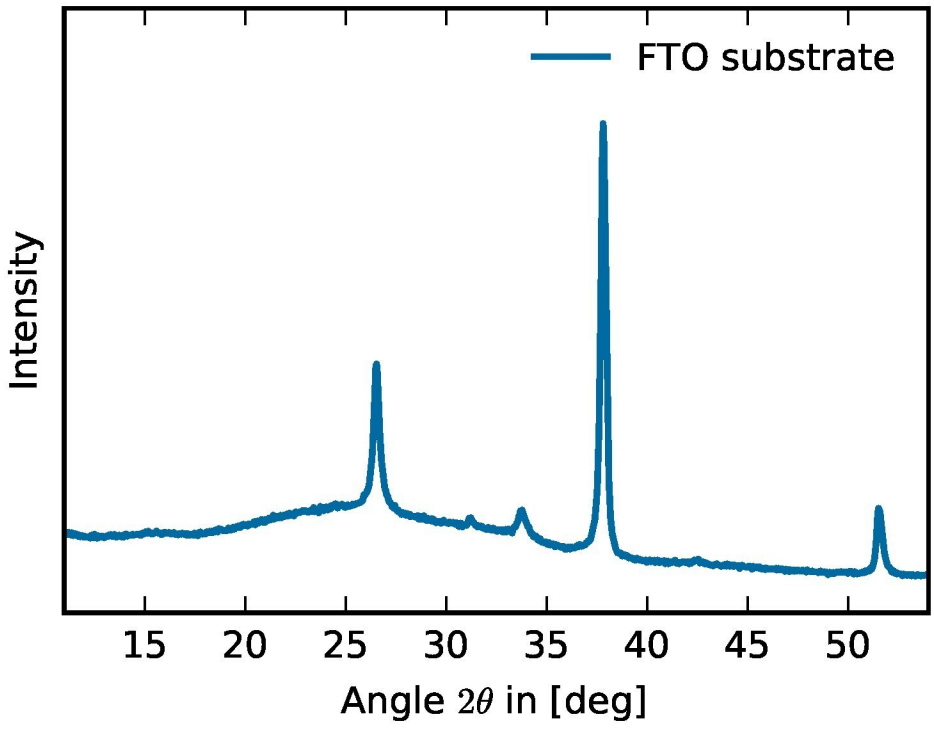

Fig. S4 XRD reference of a FTO-glass substrate.

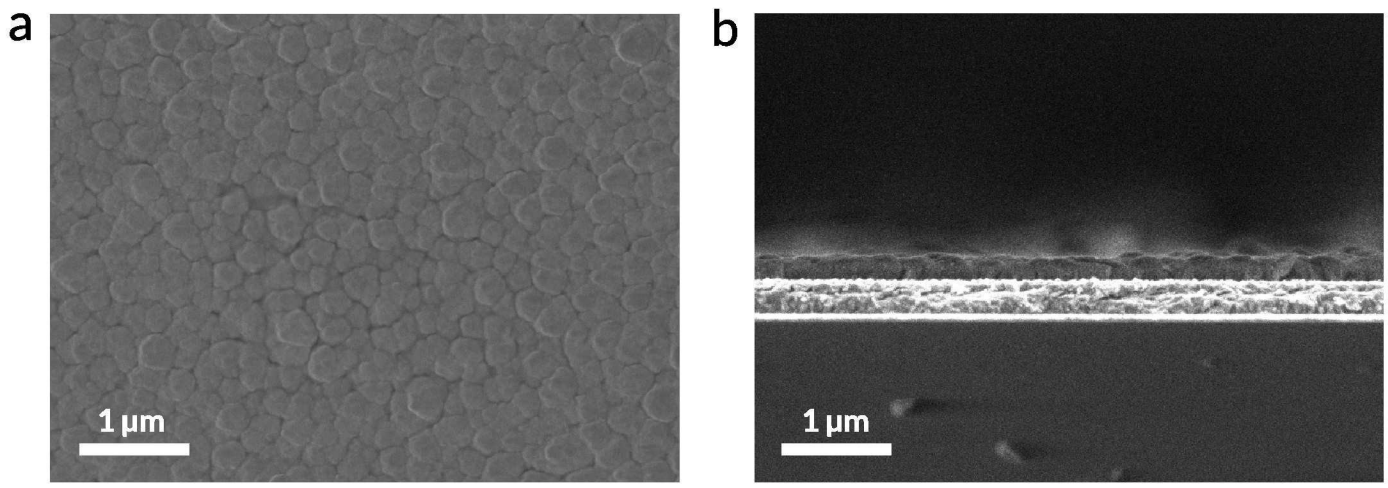

Fig. S5 (a) Top and (b) cross-sectional SEM images of an initial amorphous Sb_2S_3 layer on a FTO substrate.

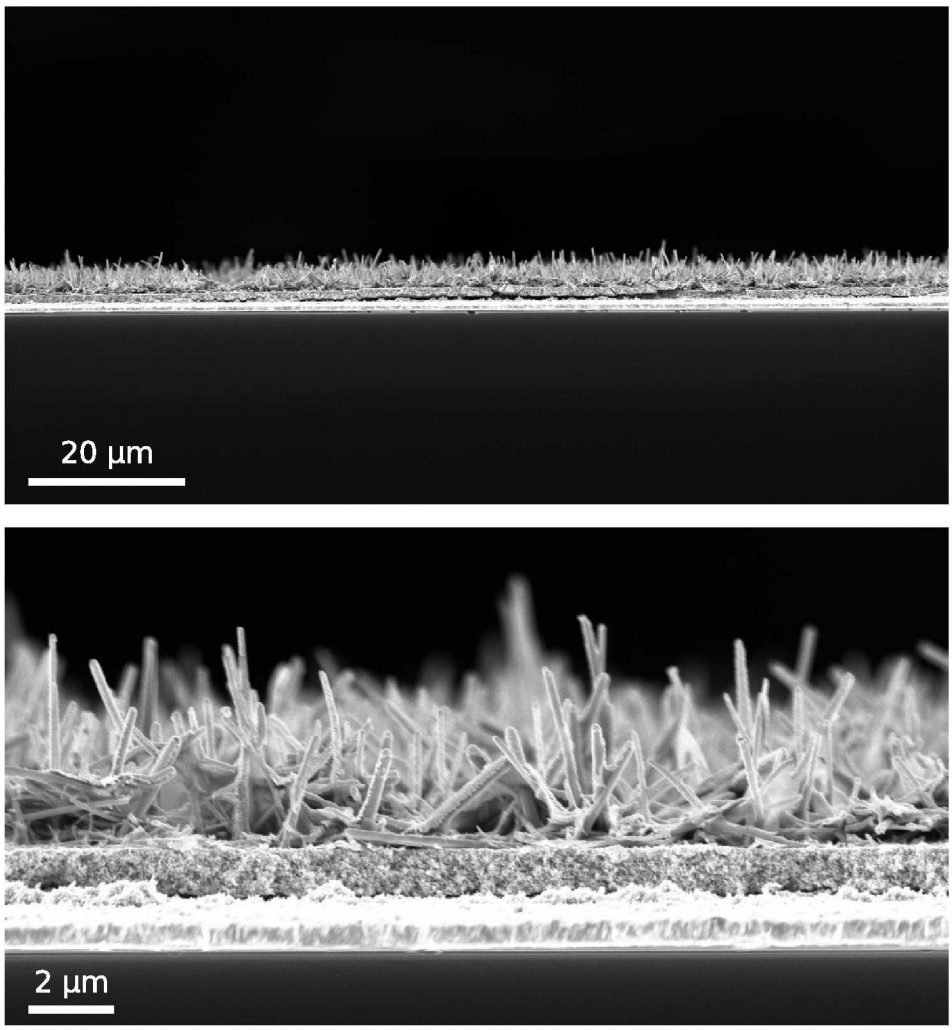

Fig. S6 Cross-sectional SEM micrographs showing the preferential orientation of SbSI crystal needles perpendicular to the substrate surface. Note that these samples had an additional mesoporous ITO layer that was deposited onto the FTO substrate prior to the formation of SbSI. This additional layer is however not necessary and was omitted in the characterised photodetectors.

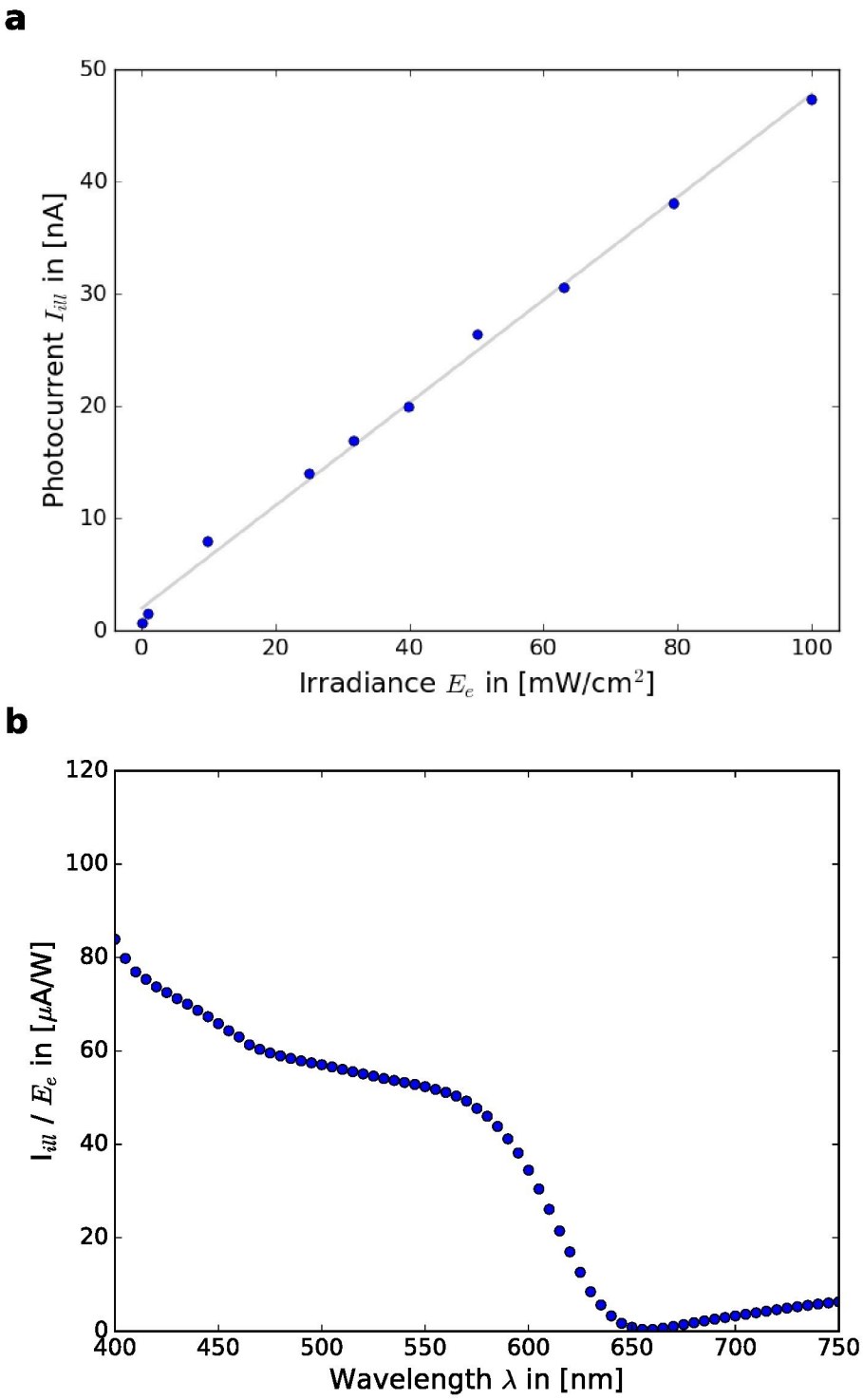

Fig. S7 (a) Photocurrent versus irradiance of the photodetector at zero bias voltage ($V_\mathrm{b} = 0\,\mathrm{V}$). (b) Spectral response of the photodetector at $V_\mathrm{b} = 0\,\mathrm{V}$.

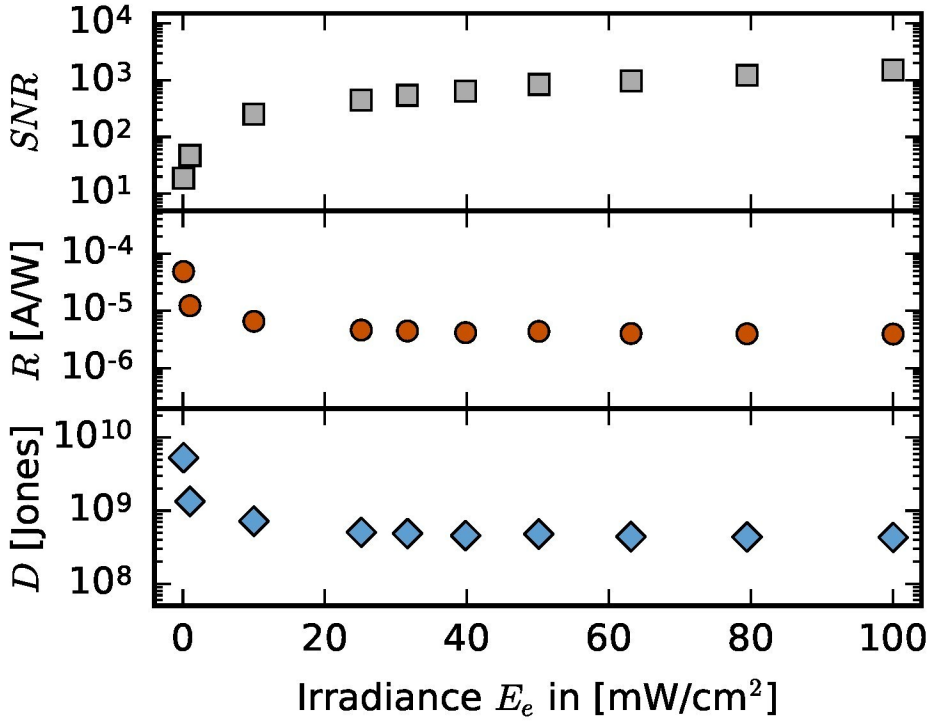

Fig. S8 Signal-to-noise ratio SNR, responsivity R and specific detectivity D^* as a function of the illumination irradiance E_e at zero bias $V_b = 0\,V$.

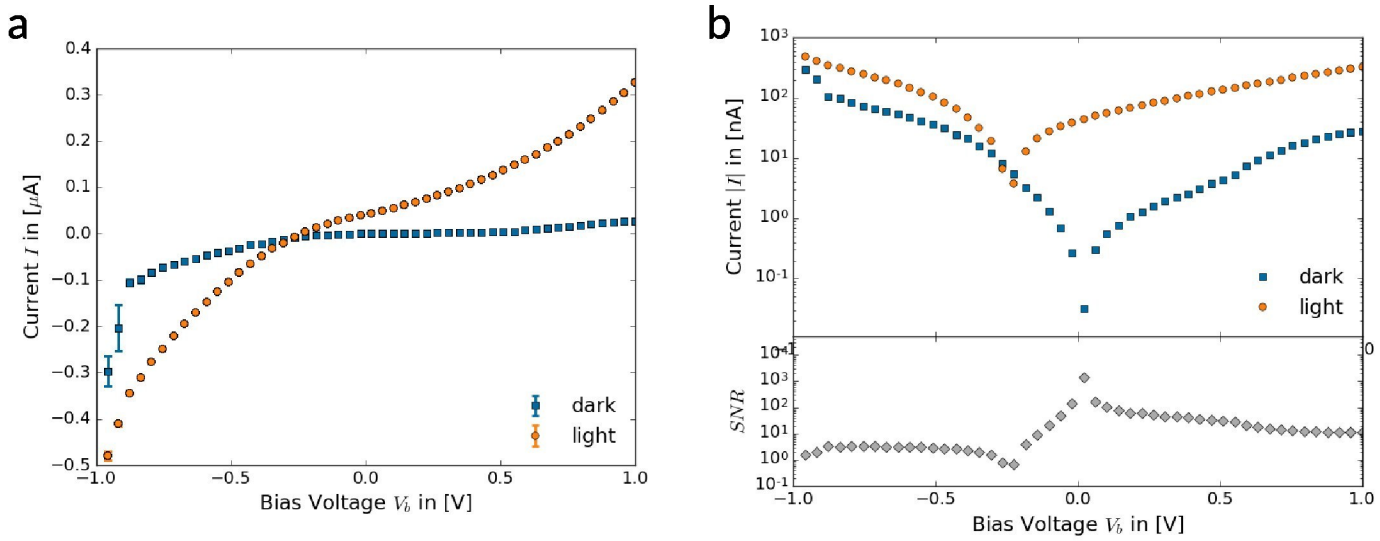

Fig. S9 (a) Linear and (b) logarithmic plot of the dark- and photocurrent of the photodetector for different bias voltages V_b. The lower frame shows corresponding signal-to-noise ratios SNR. The SNR is highest for low bias voltages, due to the low dark currents.

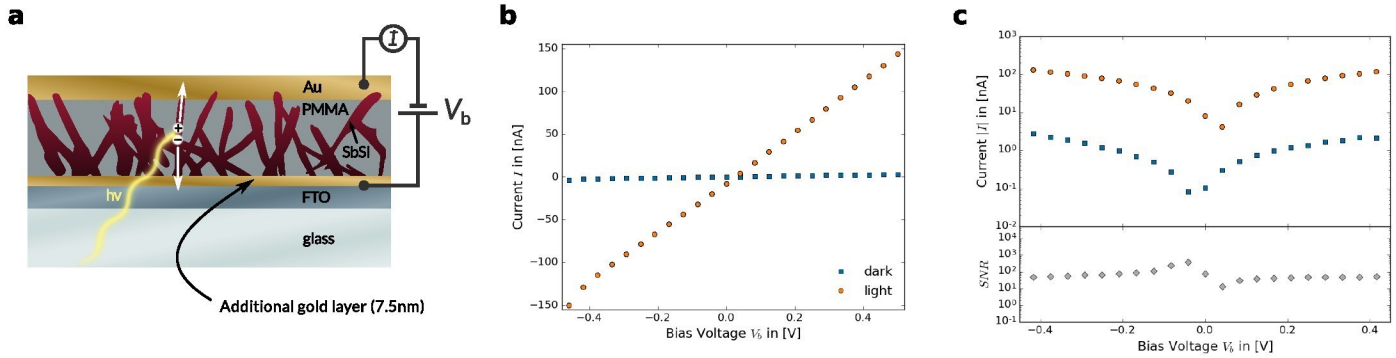

Fig. S10 (a) Schematic drawing of a photodetector incorporating an additional layer of gold (thickness 7.5 nm) on top of the FTO electrode, demonstrating the effect of symmetrical electrode work functions, compared to asymmetric work functions in Figures 4 and S9. (b) Dark- and photocurrent of the photodetector with the additional gold layer as a function of bias voltages V_b. (c) Logarithmic plot of the same measurement. The lower frame shows the corresponding signal-to-noise ratios SNR.

Table S1 Comparison of the figures of merit of SbSI, perovskite-based and a high performance CdSe-nanowire photodetector

Photodetector	I_{light} [a]	SNR	Detectivity D^*	Rise time τ_r	Fall time τ_f	Reference
"sandwich" SbSI	54 nA	1373	$6.8 \cdot 10^9$	8 ms	34 ms	This work
single-crystal SbSI	≈ 1.8 nA	700	$\approx 2.3 \cdot 10^9$	300 ms	300 ms	9
Perovskite ($CH_3NH_3PbI_3$)	≈ 10 nA	92	—	1200 ms	200 ms	2
CdSe-nanowire [b]	—	10^7	$4 \cdot 10^{13}$	350 ns	350 ns	23

[a] $V_b = 0.1$ V, $E_e = 100 \frac{mW}{cm^2}$, [b] No self-powered mode possible.